**Proceedings of the ASME 2010 International Design Engineering Technical Conferences & Computers and Information in Engineering Conference**
**IDETC/CIE 2010**
**August 15-18, 2010, Montreal, Quebec, Canada**

**DETC2010-28370**

# DISPLACEMENT AND BLOCKING FORCE PERFORMANCE OF PIEZOELECTRIC T-BEAM ACTUATORS

**Hareesh K. R. Kommepalli**
Department of Mechanical and Nuclear Engineering
The Pennsylvania State University
University, PA 16802.

**Kiron Mateti**
Department of Electrical Engineering
The Pennsylvania State University
University Park, PA 16802.

**Christopher D. Rahn** *
Department of Mechanical and Nuclear Engineering
The Pennsylvania State University
University, PA 16802.

**Srinivas A. Tadigadapa**
Department of Electrical Engineering
The Pennsylvania State University
University Park, PA 16802.

## ABSTRACT

*In this paper, we present the experimental validation of the detailed models developed for the flexural motion of piezoelectric T-beam actuators. With a T-shaped cross-section, and bottom and top flange and web electrodes, a cantilevered beam can bend in both in-plane and out-of-plane directions upon actuation. Analytical models predict the tip displacement and blocking force in both directions. Mechanical dicing and flange electrode deposition was used to fabricate six meso-scale T-beam prototypes. The T-beams were experimentally tested for in-plane and out-of-plane displacements, and out-of-plane blocking force. The analytical models closely predict the T-beam displacement and blocking force performance. A nondimensional analytical model predict that all T-beam designs for both in-plane and out-of-plane actuation, regardless of scale, have nondimensional displacement and blocking force equal to nondimensional voltage. The results from experiments are favorably compared with this theoretical prediction.*

*Send correspondence to this author: cdrahn@psu.edu, Telephone: 1 814 865 6237

## 1 INTRODUCTION

Piezoelectric actuators are used for many applications, including ultrasonic motors, micro-positioning systems, camera auto-focus lenses, structural vibration control, and control surfaces. Most piezoelectric actuators use lead zirconate titanate (PZT) because it provides large piezoelectric and electromechanical coupling factors. To produce reasonable motion, however, the 0.1% piezoelectric strain must be amplified. Stack actuators [1–3] produce larger motions by stacking electroded thin PZT disks and actuating through the thickness. In this case, the material poling, and applied voltage are in the same direction along the thickness for each block of the stack. Although, this makes use of the $d_{33}$ piezoelectric coefficient which is approximately three times larger than the $d_{31}$ coefficient used in unimorph or bimorph actuators, stack actuators with large number of layers are difficult to fabricate to produce reasonable displacements. In unimorph/bimorph actuators, two layers of material are separated by an electrode [3–6]. The unimorph has one PZT layer poled through the thickness and a passive layer. The PZT layer expands through the thickness and contracts longitudinally when an electric field is applied. The longitudinal contraction causes the unimorph to bend due to the constraining passive layer. The bimorph substitutes the passive layer with a second

active PZT layer. This produces maximum transverse displacement because each layer can be used with maximum applied field in the direction of poling. The maximum applied field in the direction opposite poling is limited to approximately one third of the coercive field to prevent depoling of the PZT. Tube actuators that produce bimorph actuation in two directions have been demonstrated at the macroscale [7] but are difficult to fabricate.

At the microscale, stack and uni/bimorph actuators are also difficult to fabricate. Although solder bonding techniques for PZT have been reported [8] stack actuators of more than a few layers have not been fabricated. Microscale actuators fabricated using AlN and ZnO [4, 9] thin films have poor performance due to the low piezoelectric coefficients of these materials. In comparison thin film PZT films exhibit much larger piezoelectric coefficients, however the quality of these films has been typically lower than of bulk PZT materials [10]. Only recently, advances in templated and textured growth of piezoelectric thin films have enabled achievement of piezoelectric coefficients in thin films that approach the values of their bulk counterparts. The challenges and opportunities relating to the integration of thin and bulk piezoelectric materials have been presented in a recent review [11]. Furthermore, the stress mismatch between the layers during the fabrication can result in variably deflected structures upon release. Thus, the performance of piezoelectric microactuators can be improved by developing novel designs that enable multidirectional displacement and provide easy fabrication by avoiding bonding of two layers.

In a previous paper we introduced the T-beam actuators [12] and developed out-of-plane models and performed preliminary optimization studies. This paper describes the in-plane and out-of-plane modeling, design, fabrication, and testing of meso-scale prototypes that are diced from bulk PZT. In this paper, we present the experimental measurements of out-of-plane and in-plane displacements and out-of-plane blocking force. The experimental results are compared with the theoretical predictions.

## 2 THE T-BEAM ACTUATOR CONCEPT

The design of a cantilevered T-beam actuator is shown in Fig. 1. The entire T-beam is PZT with electrodes deposited on the top of the web, the top of each flange, and the bottom of the flange. The PZT is poled through-the-thickness from top to bottom.

Fig. 1 shows that the T-beam actuator can be bent both in-plane and out-of-plane by selectively activating the various electrodes. The bottom electrode acts as a ground. Out-of-plane motion can be achieved by applying voltage to the web electrode or to both flange electrodes. Application of voltage to the web electrode causes the web to expand through the thickness and contracts longitudinally ($d_{31}$ piezoelectric effect). The inactive flange constrains the lower part of the T-beam, acting as the passive layer in a unimorph design, and the beam bends upward (see Fig. 1(b)). Alternatively, the two flanges contract due to flange actuation, the web resists contraction, and the T-beam bends downward (see Fig. 1(c)).

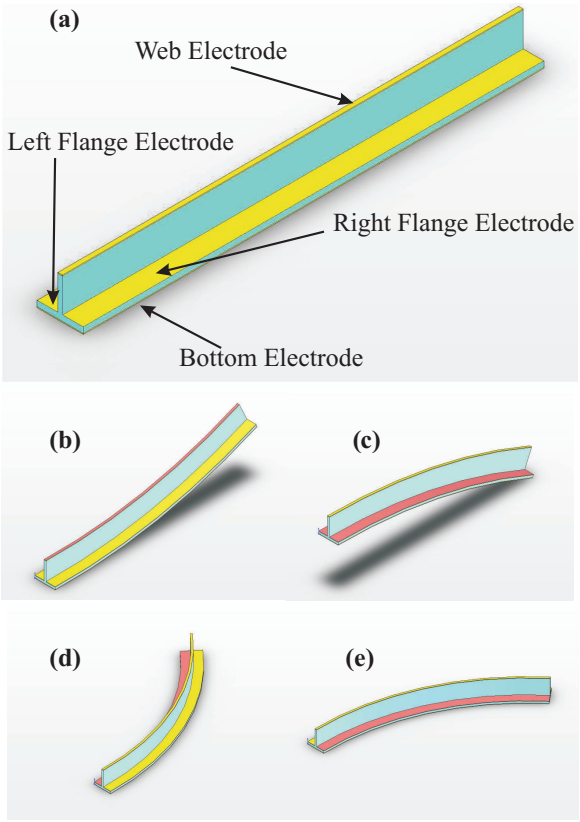


Figure 1. T-beam actuator concept: (a) As fabricated and deflected shapes when voltage is applied between (b) both flanges and bottom electrodes, (c) web and bottom electrode, (d) left flange and bottom electrode, and (e) right flange and bottom electrode.

The T-beam can also provide in-plane displacement by differential application of voltage to the two flanges. For in-plane bending the left and right flange electrodes are actuated to produce left and right bending as shown in Figs. 1(d) and 1(e), respectively. Left and right flange actuation also cause some downward out-of-plane deflection. The T-beam actuator thus eliminates bonding of two layers as in a unimorph though multiple electrodes are needed to actuate the T-beam.

## 3 ANALYTICAL MODELING

To understand the physical behavior of the T-beam actuator and optimize its performance we develop a physics based model that predicts out-of-plane and in-plane displacement and blocking force. The T-beam actuator with the web and flange elec-

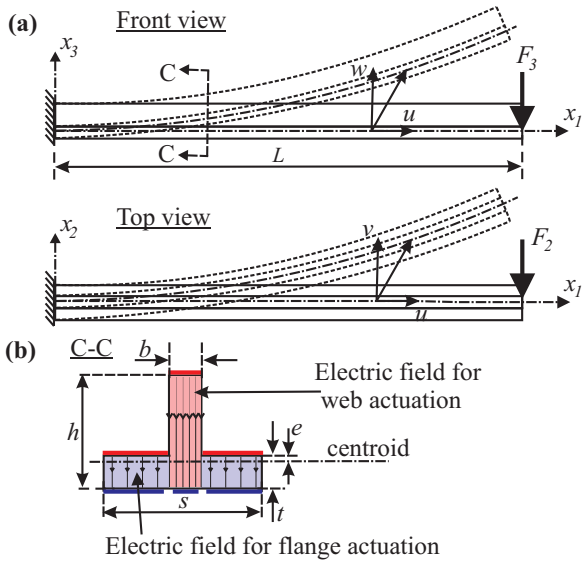


Figure 2. T-beam model: (a) the initial and deflected shape (out-of-plane (top) and in-plane (bottom)) and (b) cross section.

trodes shown in Fig. 2 is modeled as a cantilever beam using Euler-Bernoulli beam theory and assuming uniform electric field through the thickness. Fig. 2(a) shows a schematic of the initial and deflected shapes of the T-beam actuator in both out-of-plane (top) and in-plane (bottom) directions. The beam is assumed to be initially straight and lying along the longitudinal $x_1$ axis. $F_2$ and $F_3$ are the horizontal (in-plane) and vertical (out-of-plane) loads passing through the shear center of beam such that they do not cause twist. The variables $u$, $v$ and $w$ denote the displacements in the longitudinal ($x_1$), transverse in-plane ($x_2$) and transverse out-of-plane ($x_3$) directions, respectively. The cross-section of the T-beam shown in Fig. 2(b) has a flange width $s$, flange thickness $t$, web width $b$, and overall height $h$. The longitudinal axis runs through the centroid of the T-beam cross section, halfway through the cross section in the x3 direction and through the centroid at a distance

$$e = \frac{1}{2}\frac{t^2 s - t^2 b + 2tbh - bh^2}{ts - tb + bh} \tag{1}$$

below the top of the flange. As shown in Fig. 2(b), the bottom electrode is subdivided into three regions under the right and left flanges and the web. For upward out-of-plane actuation, voltage, $V$ is applied between the web and the middle electrode on the bottom of the flange. Voltage applied between right or left flange electrodes and the corresponding outer electrode on the bottom of the flange produces in-plane motion. We assume uniform and constant electric field along the $x_3$ axis through the thickness of actuator as shown in Fig. 2(b). For flange actuation, $V = (\phi_{\text{flange}} - \phi_{\text{bottom}})/t$ and we neglect the field in the web. For web actuation $V = (\phi_{\text{web}} - \phi_{\text{bottom}})/h$ and we neglect the field in the flanges.

The governing equations are obtained using the principle of virtual work. The potential energy of the T-beam actuator is

$$\begin{aligned} U_b &= \int_{V_b} \frac{E}{2}\left(u' - x_2 v'' - x_3 w''\right)^2 dV, \\ U_p &= \int_{V_p} H dV, U = U_b + U_p, \end{aligned} \tag{2}$$

where $()' = \dfrac{d()}{dx_1}$, $E$ is the Young's modulus of PZT-4, $U_b$ and $U_p$ are the potential energy of the passive region and active region, respectively, and $U$ is the total potential energy.

The electric enthalpy $H$ for the active piezoelectric material, obtained from piezoelectric constitutive equations [5, 12] and electric boundary conditions is given by

$$\begin{aligned} H =& \frac{E}{2}\left(u''\right)^2 + \frac{E}{2}{x_2}^2\left(v''\right)^2 - E x_2 u' v'' \\ &+ \left(a_2 {x_3}^2 + a_3\right)\left(w''\right)^2 + a_4 V w'' + a_5 V^2 \\ &+ \left(a_6 + a_7 x_3\right) w'' u' - \left(a_7 x_2 x_3 + a_6 x_2\right) w'' v'' \\ &+ a_8 V u' - a_8 V x_2 v'', \end{aligned} \tag{3}$$

where $e_{31} = E d_{31}$ is piezo-electric stress coefficient, and $\varepsilon_{33} = K_{33}\varepsilon_0$ is the permittivity of PZT [5]. The coefficients in Eq. (3) are given in Table 1 for web and flange actuation and $\varepsilon_{33}$ is the permittivity of PZT, $e_{31} = E d_{31}$ is the piezoelectric stress coefficient, where, $d_{31}$ is the piezoelectric strain coefficient.

Substitution of Eqs. (2) into the principal of virtual work, $\int_0^t (\delta U + F_2 \delta v(L) + F_3 \delta w(L)) dt = 0$, produces the field equations

$$\frac{d^4 w(x_1)}{dx_1^4} = 0, \frac{d^4 v(x_1)}{dx_1^4} = 0, \frac{d^2 u(x_1)}{dx_1^2} = 0, \forall x \in (0, L), \tag{4}$$

geometric boundary conditions at the fixed end

$$u(0) = 0, v(0) = 0, w(0) = 0, \frac{dv(0)}{dx} = 0, \frac{dw(0)}{dx} = 0, \tag{5}$$

Table 1. Electromechanical coefficients for web and flange actuation

| Coefficient | Web | Flange |
|---|---|---|
| $a_2$ | $\frac{1}{2}\left(E+\frac{e_{31}^2}{\varepsilon_{33}}\right)$ | $\frac{1}{2}\left(E+\frac{e_{31}^2}{\varepsilon_{33}}\right)$ |
| $a_3$ | $-\frac{e_{31}^2(2e+h-2t)^2}{8\varepsilon_{33}}$ | $-\frac{e_{31}^2(2e-t)^2}{8\varepsilon_{33}}$ |
| $a_4$ | $-\frac{e_{31}(2e+h-2t)}{2h}$ | $-\frac{e_{31}(2e-t)}{2t}$ |
| $a_5$ | $\frac{-\varepsilon_{33}}{2h^2}$ | $\frac{-\varepsilon_{33}}{2t^2}$ |
| $a_6$ | $\frac{e_{31}^2}{2\varepsilon_{33}}(2e+h-2t)$ | $\frac{e_{31}^2}{2\varepsilon_{33}}(2e-t)$ |
| $a_7$ | $-\frac{E\varepsilon_{33}+e_{31}^2}{\varepsilon_{33}}$ | $-\frac{E\varepsilon_{33}+e_{31}^2}{\varepsilon_{33}}$ |
| $a_8$ | $\frac{e_{31}}{2h}$ | $\frac{e_{31}}{2t}$ |

and the natural boundary conditions at the free end

$$\begin{aligned}
&E(A_b+A_p)\frac{du(L)}{dx}+a_8A_pV=0,\\
&E(I_{p2}+I_{b2})\frac{d^2v(L)}{dx_1^2}-a_8A_{p2}V=0,\\
&E(I_{p2}+I_{b2})\frac{d^3v(L)}{dx_1^3}-F_2=0,\\
&(EI_{b3}+2a_2I_{p3}+2a_3A_p)\frac{d^3w(L)}{dx_1^3}-F_3=0,\\
&(EI_{b3}+2a_2I_{p3}+2a_3A_p)\frac{d^2w(L)}{dx_1^3}+a_4A_pV=0,
\end{aligned} \tag{6}$$

where $(A_p,A_b)$, $(A_{p2},A_{b2})$, $(I_{p2},I_{b2})$, and $(I_{p3},I_{b3})$ are the cross-sectional area, first moment of area, and second moment of area of the active and passive regions, respectively, about the neutral axis as given in Tab. 2.

The solutions of Eqs. (4) are

$$\begin{aligned}
u(x_1)&=b_1x_1+b_0,\\
v(x_1)&=c_3x_1^3+c_2x_1^2+c_1x_1+c_0,\\
w(x_1)&=d_3x_1^3+d_2x_1^2+d_1x_1+d_0.
\end{aligned} \tag{7}$$

The 10 unknown coefficients $b_j$ , $c_i$, $d_i$ are solved analytically using the 10 boundary conditions to obtain

$$\begin{aligned}
w(x_1)=&\frac{-(LF_3+a_4VA_p)x_1^2}{2(2a_2I_{p3}+2a_3A_p+E_pI_{b3})}\\
&+\frac{F_3x_1^3}{6(2a_2I_{p3}+2a_3A_p+E_pI_{b3})},\\
v(x_1)=&\frac{(-LF_2+a_8VA_{p2})x_1^2}{2E_p(I_{p2}+I_{b2})}+\frac{F_2x_1^3}{6E_p(I_{p2}+I_{b2})}.
\end{aligned} \tag{8}$$

The tip displacements obtained by substituting $x_1=L$ in Eq. (8) are

$$\begin{aligned}
v(L)=&-\frac{L^3F_2}{3E_p(I_{p2}+I_{b2})}+\frac{a_8A_{p2}L^2V}{2E_p(I_{p2}+I_{b2})},\\
w(L)=&-\frac{L^3F_3}{3(2a_2I_{p3}+2a_3A_p+E_pI_{b3})}\\
&-\frac{a_4A_pL^2V}{2(2a_2I_{p3}+2a_3A_p+E_pI_{b3})}.
\end{aligned} \tag{9}$$

The free tip displacements, $v_f$ and $w_f$, defined as the displacement at the tip of actuator when the applied force $F_2$ and $F_3$ equal to zero are

$$\begin{aligned}
v_f&=\frac{a_8A_{p2}L^2V}{2E_p(I_{p2}+I_{b2})},\\
w_f&=-\frac{a_4A_pL^2V}{2(2a_2I_{p3}+2a_3A_p+E_pI_{b3})},
\end{aligned} \tag{10}$$

where $F_2$=$F_3$=0 in Eq. (9). The blocking forces,

$$\begin{aligned}
F_{2b}&=\frac{3a_8A_{p2}V}{2L},\\
F_{3b}&=-\frac{3a_4A_pV}{2L}
\end{aligned} \tag{11}$$

constrain the tip displacements $v(L)$=$w(L)$=0 in Eq. (9).

### 3.1 Nondimensional modeling

We reduce the parametric model to a simple linear relationship between the nondimensional voltage and the nondimensional displacements and blocking forces. In this way, all of the obtained experimental data can be shown on one plot, regardless of the device parameters. The nondimensional (starred) parameters

$$x_1^*=\frac{x_1}{L},w^*=\frac{w}{L},v^*=\frac{v}{L}, \tag{12}$$

Table 2. Cross-sectional area, first moment of area, and second moment of area for web, flange and, single flange actuation

| Constant | Web | Flange | Single flange |
|---|---|---|---|
| $A_b$ | $t(s-b)$ | $bh$ | $\frac{(2h-t)b+st}{2}$ |
| $A_p$ | $bh$ | $t(s-b)$ | $\frac{(s-b)t}{2}$ |
| $A_{p2}$ | 0 | 0 | $\frac{t\left(s^2-b^2\right)}{8}$ |
| $I_{b2}$ | $\frac{t}{12}\left(s^3-b^3\right)$ | $\frac{b^3h}{12}$ | $\frac{(2h-t)b^3+s^3t}{24}$ |
| $I_{p2}$ | $\frac{b^3h}{12}$ | $\frac{t}{12}\left(s^3-b^3\right)$ | $\frac{t\left(s^3-b^3\right)}{24}$ |
| $I_{b3}$ | $\frac{(s-b)t^3}{12}$ $+A_b\left(e-\frac{t}{2}\right)^2$ | $\frac{bh^3}{12}$ $+A_b\left(e-t+\frac{h}{2}\right)^2$ | $I_{p3}+\frac{bh^3}{12}$ $+bh\left(e-t+\frac{h}{2}\right)^2$ |
| $I_{p3}$ | $\frac{bh^3}{12}$ $+A_p\left(e-t+\frac{h}{2}\right)^2$ | $\frac{(s-b)t^3}{12}$ $+A_p\left(e-\frac{t}{2}\right)^2$ | $\frac{(s-b)t^3}{24}$ $+A_p\left(e-\frac{t}{2}\right)^2$ |

are introduced into Eq. 4 to produce

$$w^*(1) = F_3^* + V_3^*, v^*(1) = F_2^* + V_2^*, \tag{13}$$

where the nondimensional forces and voltages in the out-of-plane and in-plane directions are

$$F_2^* = -\frac{\kappa}{3\gamma}, F_3^* = -\frac{\beta}{3\alpha}, V_2^* = -\frac{\psi}{2\gamma}, V_3^* = -\frac{\tau}{2\alpha}, \tag{14}$$

with the parameters

$$\begin{aligned} &\alpha = 1 + \frac{2a_2 I_{p3}}{EI_{b3}} + \frac{2a_3 A_p}{EI_{b3}}, \beta = \frac{F_3 L^2}{EI_{b3}}, \tau = \frac{a_4 V A_p L}{EI_{b3}}, \\ &\gamma = 1 + \frac{I_{p2}}{I_{b2}}, \kappa = \frac{F_2 L^2}{EI_{b2}}, \psi = -\frac{a_8 V A_{p2} L}{EI_{b2}}, \end{aligned} \tag{15}$$

From Eq. (13) the nondimensional free tip displacements

$$v_f^* = V_2^*, w_f^* = V_3^*, \tag{16}$$

and the non-dimensional blocking forces

$$F_{2b}^* = -V_2^*, \; F_{3b}^* = -V_3^*. \tag{17}$$

## 4 FABRICATION PROCESS

A schematic illustration of the T-beam fabrication process using a precision dicing saw and photolithography is shown in Fig. 3. A K & S Model 980 precision dicing saw defines web regions on a finely polished 25.4 mm X 25.4 mm X 1 mm PZT-4 substrate which has been electroded with a layer of Cr/Au shown in Fig. 3(a-b). The saw uses a 100 $\mu$m Nickel blade coated with 3-6 $\mu$m diamond grit. Figure 3(c) shows the bottom electrodes patterned and etched using photolithography and wet etching. The high aspect ratio T-beams are spray coated with Shipley 1805 photoresist, and the flange electrodes are then aligned

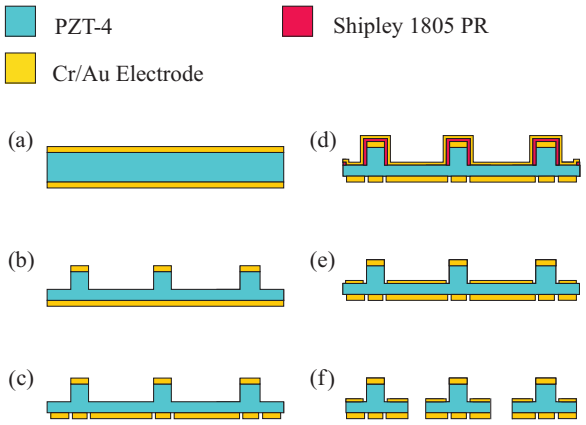


Figure 3. Schematic illustration of T-beam fabrication: (a) start with 1mm thick bulk PZT-4 with Cr/Au coating, (b) dice to form web regions, (c) etch bottom electrodes, (d) spray photoresist pattern and evaporate Cr/Au for flange electrodes, (e) lift-off photoresist to form flange electrodes, (f) release individual T-beams by dicing.

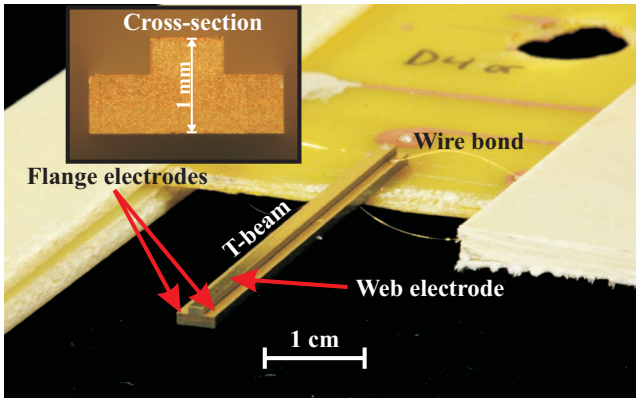


Figure 4. Photograph of a fabricated and mounted T-beam (Device 4) actuator.

and patterned. A layer of 15 nm Cr and 150 nm Au is vacuum evaporated onto the substrate using a planetary sample holder on an electron beam evaporator with a MDC Mighty Source™as shown in Fig. 3(d). An ultrasonic acetone bath was used to perform the liftoff procedure removing photoresist and gold from the undesired areas as shown in Fig. 3(e). The T-beams were finally released by dicing (see Fig. 3(f)). The T-Beams are then packaged onto custom designed PCBs and wire bonded using a K&S Model 4524 wire bonding machine. In total, 6 independent electrodes (3 on top and 3 on bottom) enable actuation of the T-beam in both out-of-plane and in-plane directions. The web regions and flange regions have identical polarization which allows actuation using one high voltage amplifier and appropriate circuitry.

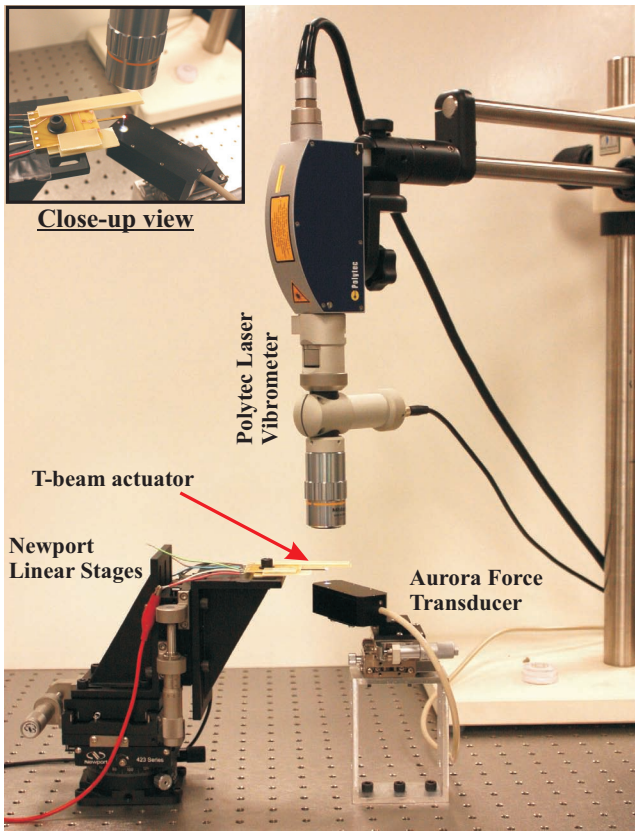


Figure 5. Photograph of experimental set-up to measure displacement and blocking force of T-beam actuators.

## 5 PROTYPING AND EXPERIMENTAL SETUP

Six devices are built with the different configurations as listed in Tab. 3. Five of the devices have different flange thicknesses and approximately same length and web width except for first one which had its tip broken off during fabrication. Figure 4 shows the picture of fabricated and mounted Device 4. The inset zooms in on the cross-section of T-beam at the tip. The 0.8 mm thick FR4 circuit board is attached along its edges to a thicker 1.6 mm FR4 base which then is attached to linear stages that allow precise positioning of the actuator. High resolution pictures of the cross-section, top-view, and bottom view of each device were used to measure the various geometric parameters with a precision of approximately $\pm 20\ \mu$m in cross-sectional dimensions and $\pm 50\ \mu$m in length. The material properties of PZT-4 used for the fabricated T-beams are given in Tab. 4.

Table 3. Fabricated prototype parameters

| Device | Length $L$ (mm) | Total width $s$ ($\mu$m) | Flange thickness $t$ ($\mu$m) | Height $h$ ($\mu$m) | Web width $b$ ($\mu$m) |
|---|---|---|---|---|---|
| 1 | 14.6 | 2012 | 134 | 1000 | 765 |
| 2 | 20.4 | 2008 | 298 | 1000 | 774 |
| 3 | 20.1 | 2000 | 417 | 1000 | 764 |
| 4 | 20.4 | 1993 | 612 | 1000 | 756 |
| 5 | 21.3 | 2017 | 788 | 1000 | 770 |
| 6 | 20.7 | 1995 | 320 | 1000 | 512 |

Table 4. PZT-4 material properties

| Description | |
|---|---|
| Youngs modulus of PZT, $E$ (GPa) | 78 |
| Piezoelectric strain coefficient, $d_{31}$ (C/N) | -122e-12 |
| Permittivity of PZT, $\varepsilon_{33}$ ($C^2/(Nm^2)$) | 1.15e-08 |

The experimental setup used to measure the displacement and blocking force of the actuators is shown in figure 5. A model OFV5000 Polytec laser vibrometer controller with OFV534 sensor head measures the displacement with a measuring spot size of 20 $\mu$m. A 3-axis Newport linear stage with micrometer screws accurately positions the T-beam so that the laser is precisely focused at the desired location. An Aurora 402A force transducer with a 1 mm diameter glass tube sensing tip was used to measure the blocking force. The force transducer has a resolution of 10 $\mu$N and can measure up to ±500 mN. The force transducer was mounted on two Aurora linear stages to allow positioning the sensor tip at the desired location on the T-beam. A model 609E-6 Trek amplifier generates the desired voltages for actuating the T-beams.

## 6 EXPERIMENTAL TESTING AND VALIDATION

The six independent electrical connections on the fabricated T-beams enable web, flange, right flange or left flange actuation to produce out-of-plane and in-plane motions. Blocking force measurements are performed only for web and flange actuations due to the difficulty in measuring transverse forces.

A triangle wave signal at 1 Hz frequency (total 10 cycles) was used to actuate the T-beam such that the electric field $\phi$ is always in the direction of poling. The experiment was repeated for peak electric fields of 0.1, 0.2, 0.3, 0.4, 0.5 V/$\mu$m for both displacement and blocking force measurements. The peak voltage applied was $V = \phi h$ for web actuation and $V = \phi t$ for flange actuation and the un-actuated electrodes were allowed to float. To account for the compliance of force sensor and FR4 mounting, displacement measurements were taken at the tip and base of the T-beam actuator during blocking force measurements.

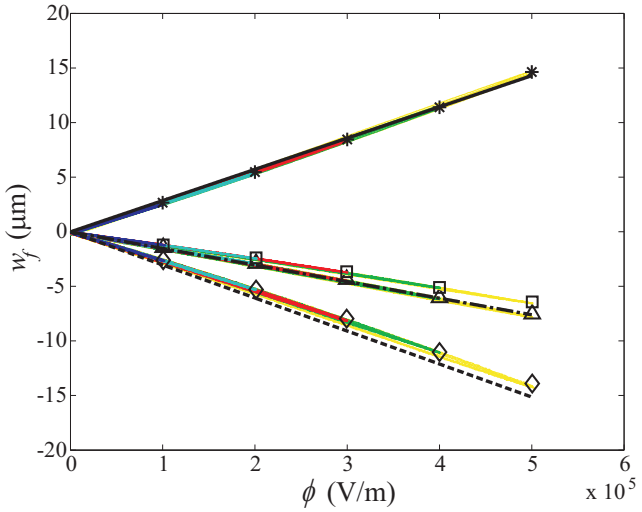


Figure 6. Free tip out-of-plane displacement $w_f$ versus applied electric field $\phi$ versus for Device 3: Theoretical (solid - web actuation, dashed - flange actuation, dashdot - right or left flange actuation) and experimental (star - web actuation, diamond - flange actuation, square - left flange, and triangle - right flange).

Figure 6 shows the out-of-plane free tip displacements $w_f$ of device 3 for different actuations. The yellow, green, red, cyan blue colored lines are the experimental data under triangle wave excitation for applied electric field of 0.5, 0.4, 0.3, 0.2, 0.1 V/$\mu$m, and the symbols are averages over 10 cycles. Similarly, Fig. 7 shows the experimental and analytical in-plane free tip displacement $v_f$ versus applied electric field $\phi$. The data shows that the analytical predictions closely match the displacement magnitude and trend for the T-beam actuator. The experimental T-beams are not rigidly clamped at the base because the FR4 circuit board is thinner and softer than the T-beam. The electrodes extend all the way to the end of the beam. Sixty percent of the ``clamped´´region is included in the beam length to model this effect. The experimental displacements show a linear relationship with the applied field. Web and both flange actuation produce similar displacements in opposite directions. Single flange actuation produces less out-of-plane displacement and, as expected, the left and right flange actuation cases produce similar displacements.

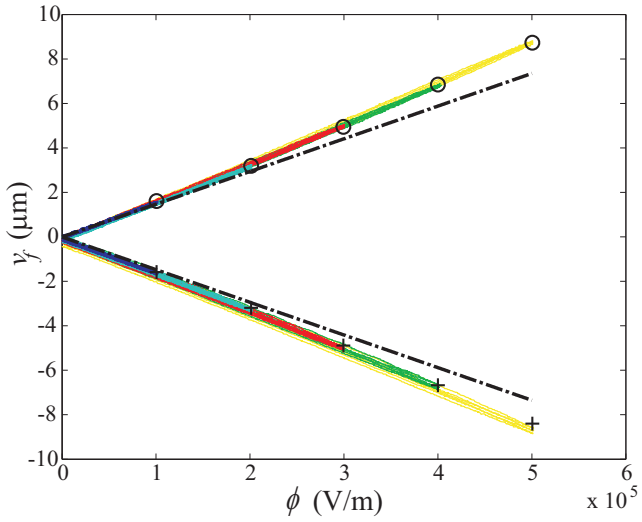


Figure 7. In-plane tip displacement, $v_f$ versus applied electric field, $\phi$ for Device 3: theoretical (dashdot - Right flange (top), left flange (bottom)) and experimental (plus - left flange, circle - right flange).

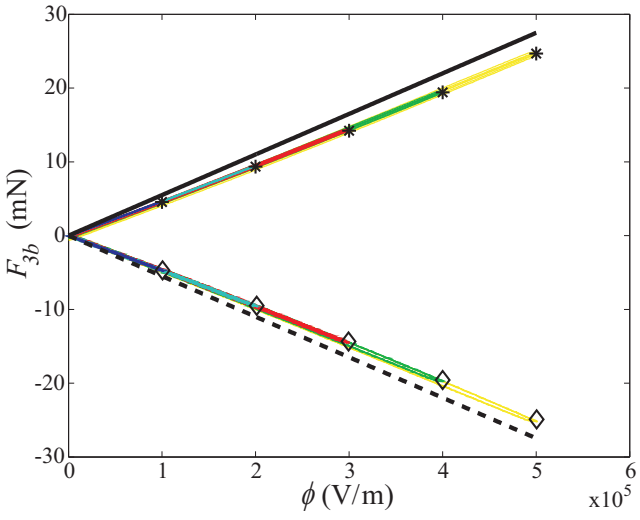


Figure 8. Tip force, $F_3$ versus applied electric field $\phi$ for Device 3: Theoretical (solid - web actuation, dashed - flange actuation) and experimental (star - web actuation, diamond - flange actuation).

The compliance of the FR4 circuit board also affected the blocking force measurements. As as result, perfect clamped boundary conditions are not realized. Accordingly, the experimental blocking force is

$$(F_{3b})_{\text{exp}} = (F_3)_{\text{exp}} + \frac{3\,(2\,a_2 I_{p3} + 2\,a_3 A_p + E_p I_{b3})\,w_{\text{exp}}}{L^3}, \quad (18)$$

where, $w_{\text{exp}}$ is the measured displacement of T-beam with tip force. Figure 8 shows the experimental and theoretical out-of-plane blocking force for web and flange actuation.The analytical model predicts the trend accurately but slightly overpredicts the magnitude. The results are linear with applied field and the web and flange actuation produce similar blocking forces at similar field. It should be noted, however, that flange actuation uses less voltage because the flange is thinner than the web.

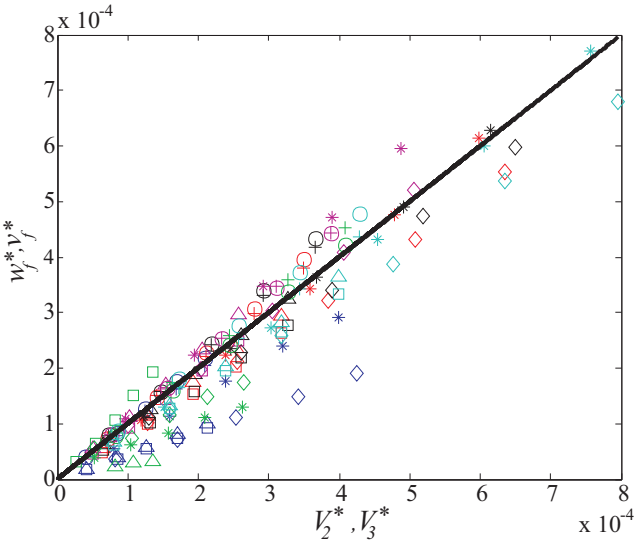


Figure 9. Non-dimensional displacement, $v_f^*$, $w_f^*$ versus non-dimensional voltage, $V_2^*$, $V_3^*$ for Devices 1 - 6: Theoretical (solid) and experimental (star - web actuation, diamond - flange actuation, square or plus - left flange, triangle or circle - right flange actuation).

Figure 9 shows the nondimensional analytical and experimental displacements $v_f^*$, $w_f^*$ versus nondimensional voltage $V_2^*$ and $V_3^*$ for Devices 1 - 6. Nondimensionalization allows the in-plane and out-of-plane displacement results for all the devices in all actuation modes to be plotted against the one theoretical line. Different symbols denote different types of actuation and each color represents a different device. From the plot, it can seen, that the analytical model in general closely predicts the trend and magnitude of all the devices. A linear fit to the data has a slope of 43.3°, within 3.8% of the analytical slope of 45°. The 95% confidence interval has a lower limit of 42.5° and a upper limit of 44.1°. Device-1 (blue) has inferior flange electrodes that produce poor performance in flange actuation. Device 4 (magenta)

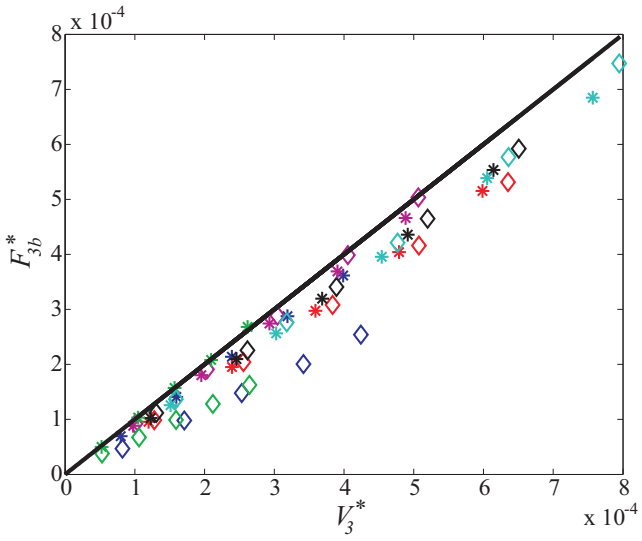


Figure 10. Non-dimensional blocking force $F^*_{3b}$ versus nondimensional voltage $V^*_3$ for Devices 1 to 6: Theoretical (solid) and experimental (star - web actuation, diamond - flange actuation).

in web actuation, however, produced higher displacements than predicted by theory.

Figure 10 shows the dimensionless blocking force $F^*_{3b}$ for Devices 1 - 6 versus dimensionless voltage $V^*_3$. The best fit line for the experimental data has a slope of 41.2°, within 8% of the theoretical slope of 45°. The 95% confidence interval of slope has a lower limit of 40.5° and a upper limit of 41.9°. Again, the flange actuation cases slightly underperform web actuation, probably due to incomplete coverage of the flanges by the deposited electrodes.

## 7 FUTURE WORK

The analytical model developed closely predicts the T-beam performance. We plan to use this analytical model to optimize the displacement and blocking force performance of T-beam actuators. Also, we plan to compare its optimized performance with the state of the art actuators like unimorph actuator. Furthermore, T-beams are to be studied for dynamic response.

## 8 CONCLUSIONS

In this paper, an analytical model is developed that predicts displacement and blocking force in both in-plane and out-of-plane directions. Six T-beam prototypes are built using mechanical dicing and electrode deposition and experimentally tested for in-plane and out-of-plane displacement and out-of-plane blocking force. Analytical models closely predict the T-beam displacement and blocking force performance.

## 9 ACKNOWLEDEMENTS

The authors would like to thank the Air Force Office of Scientific Research and Dr. Victor Giurgiutiu for their support of this work under grant # FA9550-07-1-0367.

## REFERENCES

[1] Giurgiutiu, V., and Rogers, C. A., 1996. "Energy based comparison of solid state induced strain actuators". *Journal of Intelligent Material Systems and Structures,* **7**, January, pp. 4–14.

[2] Giurgiutiu, V., Rogers, C. A., and Chaudhry, Z., 1997. "Design of displacement amplified induced-strain actuators for maximum energy output". *Journal of Mechanical Design,* **119**, December, pp. 511–517.

[3] Uchino, K., 2000. *Ferroelectric devices*. Marcel Dekker, New York.

[4] Perin, G., 2001. "Micromachined piezoelectrically actuated flextensional transducers for high resolution printing and imaging". *IEEE Ultrasonics Symposium*, pp. 921–924.

[5] Basak, S., Raman, A., and Garimella, S. V., 2005. "Dynamic response optimization of piezoelectrically excited thin resonant beams". *Journal of Vibration and Acoustics,* **127**, pp. 18–27.

[6] Wang, Q.-M., Du, X.-H., Xu, B., and Cross, L. E., 1999. "Electromechanical coupling and output efficiency of piezoelectric bending actuators". *IEEE Transactions on Ultrasonics, Ferroelectrics, and Frequency control,* **46**(3), pp. 1947–1955.

[7] Berg, M., Hagedorn, P., and Gutschmidt, S., 2004. "On the dynamics of piezoelectric cylindrical shells". *Journal of Sound and Vibration,* **274**(1-2), July, pp. 91–109.

[8] Goyal, A., Cheong, J., and Tadigadapa, S. A., 2004. "Tin-based solder bonding for mems fabrication and packaging applications". *Journal of Micromechanics and Microengineering,* **14**(6), June, pp. 819–825.

[9] Cheong, J., Goyal, A., Tadigadapa, S. A., and Rahn, C. D., 2005. "Fabrication and performance of a flextensional microactuator". *Journal of Micromechanics and Microengineering,* **15**, pp. 1947–1955.

[10] Gross, S. J., Tadigadapa, S. A., Jackson, T. N., Trolier-McKinstry, S., and Zhang, Q. Q., 2003. "Lead-zirconate-titanate based piezoelectric micromachined switch". *Applied Physics Letters,* **83**(1), July, pp. 174–176.

[11] Tadigadapa, S. A., and Mateti, K., 2009. "Piezoelectric mems sensors: state-of-the-art and perspectives". *Measurement Science and Technology,* **20**(10), pp. 1–30.

[12] Kommepalli, H. K. R., Hirsh, A. D., Rahn, C. D., and Tadigadapa, S. A., 2008. "Piezoelectric t-beam microac-

tuators". *Proceedings of ASME 2008 International Design Engineering Technical Conference & Computers and Information in Engineering Conference*, August.